RESEARCH ARTICLE
SPACE PHYSICS: IONOSPHERIC PHYSICS

Earth and Planetary Physics
6: 474–486, 2022
doi: 10.26464/epp2022043

Numerical study on matching conditions of Langmuir parametric instability and the formation of Langmuir turbulence in ionospheric heating

MoRan Liu[1], Chen Zhou[1*], Ting Feng[1], Xiang Wang[2*], and ZhengYu Zhao[1]

[1]Department of Space Physics, School of Electronic Information, Wuhan University, Wuhan 430072, China;

[2]School of Computer Science and Information Engineering, Hubei University, Wuhan 430011, China

Key Points:

- The frequency and wavevector matching conditions are investigated in detail to show the time evolution of the initial parametric decay instability stage and the cascade process.
- Caviton collapse and strong Langmuir turbulence result in a discrete wavenumber spectrum extending to a continuous one.
- The effects of ion cavitons on Langmuir turbulence shown in the evolution of the spectra are analyzed as a complement to previous studies.

Citation: Liu, M. R., Zhou, C., Feng, T., Wang, X., and Zhao, Z. Y. (2022). Numerical study on matching conditions of Langmuir parametric instability and the formation of Langmuir turbulence in ionospheric heating. *Earth Planet. Phys.*, *6*(5), 474–486. http://doi.org/10.26464/epp2022043

Abstract: Parametric decay instability (PDI) is an important process in ionospheric heating. This paper focuses on the frequency and wavevector matching condition in the initial PDI process, the subsequent cascade stage, and the generation of strong Langmuir turbulence. A more general numerical model is established based on Maxwell equations and plasma dynamic equations by coupling high-frequency electromagnetic waves to low-frequency waves via ponderomotive force. The primary PDI, cascade process, and strong Langmuir turbulence are excited in the simulation. The matching condition in the initial PDI stage and cascade process is verified. The result indicates that the cascade ion acoustic wave may induce or accelerate the formation of cavitons and lead to the wavenumber spectrum being more enhanced at $2k_L$ (where k_L is the primary Langmuir wavenumber). The wavenumber spectra develop from discrete to continuous spectra, which is attributed to the caviton collapse and strong Langmuir turbulence.

Keywords: ionospheric electromagnetic propagation; parametric decay instability; cascade; Langmuir turbulence

1. Introduction

Parametric instability in ionospheric heating by powerful high-frequency radio waves has been investigated both theoretically and experimentally for many years (Fejer, 1979; Stenflo, 1985; Leyser, 1991; Song B et al., 1995; Kuo SP, 2014; Akbari et al., 2017). Langmuir parametric instability, which is related to Langmuir wave excitation, is excited below the O-mode wave reflection point. In ionospheric heating, parametric decay instability (PDI; Kuo SP, 2015) and oscillating two-stream instability (Kuo SP et al., 1997) are two typical types of parametric instability. In PDI, the pump wave decays into a Langmuir wave and an ion acoustic wave. This three-wave coupling process is governed by the frequency and wavevector matching conditions: $\omega_p = \omega_L + \omega_{IA}$ and $k_p = k_L + k_{IA}$, where p, L, and IA denote the pump wave, Langmuir wave, and ion acoustic wave, respectively. Another indispensable condition for PDI excitation in ionospheric heating is that the pump electric field should exceed the PDI threshold (Bryers et al., 2013). If the two conditions above are both satisfied, the secondary PDI process can be excited, and the Langmuir wave decays into a daughter Langmuir wave and an ion acoustic wave as a pump wave. This cascade process leads to the generation of Langmuir turbulence (DuBois et al., 1990, 2001; Stubbe et al., 1992; Cheung et al., 2001).

The high-frequency-enhanced plasma lines and high-frequency-enhanced ion lines observed by incoherent scatter radar in ionospheric heating (Blagoveshchenskaya et al., 2015, 2017; Wang X et al., 2016; Wang X and Zhou C, 2017) are considered direct evidence of parametric instability excitation. Carlson et al. (1972) observed a strong narrow line displaced below the high frequency by the frequency of the ion acoustic waves in the plasma, a line near ion acoustic waves, and other weak lines near high frequency at Arecibo. High-frequency-enhanced plasma lines have also been observed by EISCAT radar (Hagfors et al., 1983; Stubbe et al., 1992; Westman et al., 1995; Rietveld et al., 2000). Kuo SP (2001, 2003) observed and studied the cascade lines in parametric instability spectra. In addition, Bryers et al. (2013)

Correspondence to: C. Zhou, chenzhou@whu.edu.cn
X. Wang, wangxiang.whu@whu.edu.cn
Received 18 MAR 2022; Accepted 29 JUN 2022.
Accepted article online 29 JUL 2022.

investigated the thresholds of ionospheric plasma instabilities by observing the plasma lines with different effective radiated powers at EISCAT.

The weak turbulence approximation (WTA) was presented to explain the expanded spectra in the ionospheric heating experiment (Perkins and Kaw, 1971; Fejer and Kuo YY, 1973). Hanssen et al. (1992) compared solutions of WTA with solutions of the Zakharov system and found that the Zakharov system was closer to the observations in experiments. Unlike the WTA, the strong Langmuir turbulence (SLT) theory, which was presented by DuBois et al. (1988, 1990), indicated that the weak Langmuir turbulence theory has a very limited validity range close to the reflection level and should be replaced by the SLT theory in this region. The SLT theory also showed that ion caviton collapse could be generated, which is related to oscillating two-stream instability. The irregularities can be excited in turbulence process with meter scale, which is smaller than in Natural excitation process with kilometer scale (Liu et al., 2021). The irregularities can effect the wave propagation (Jiang et al., 2020).

The saturation spectrum in ionospheric heating has been explained qualitatively by the WTA and SLT theories in previous studies; however, there are still some unsolved open questions. The linear matching condition of frequency and wavevector has not been verified theoretically, in which the nonlinear process should be considered. Moreover, the evolution of the wavenumber spectrum has not been studied. The details of Langmuir turbulence formation related to cascade and caviton collapse are not clear. In this study, we aim to verify and investigate the matching conditions to give a detailed account of Langmuir turbulence formation, which will cover the entire stage of parametric instability in ionospheric heating, by using the numerical results. Although some preliminary results can be found in Feng T et al. (2018), more detailed results are presented in this work. The matching conditions are verified from the frequency and wavevector spectra during the initial PDI stage and the cascade process. Further, the effects of ion cavitons on Langmuir turbulence shown in the evolution of the spectra are analyzed.

2. Modeling of PDI

Many authors have used modeling of PDI by the extended or generalized Zakharov model for ionospheric heating studies (DuBois et al., 1988, 1990, 1993). Eliasson and Stenflo (2008) proposed a generalized driven and damped Zakharov system that couples high-frequency electromagnetic waves to low-frequency electrostatic waves via ponderomotive force. In this model, the generation of Langmuir turbulence is simulated by means of a one-dimensional full-scale model (Eliasson and Stenflo, 2008, 2010). Many studies have presented a model of electromagnetic wave propagation in the ionosphere based on the Maxwell equations (Dahl and Murphree, 1972; Rush, 1986; Nguyen et al., 2015). In our one-dimensional model, the electromagnetic wave is assumed to be transmitted vertically into the ionosphere, with spatial variations only in the z-direction (Cartesian coordinate system, where x, y, z denote geographic east, north, and vertically upward components, respectively). According to the Coulomb gauge condition $\nabla\cdot\boldsymbol{A}=0$, or $A_z=0$ in one dimension, the vector function $\boldsymbol{A}(z,t)$ and the scalar function $\varphi(z,t)$ are introduced in Equation (1):

$$\begin{cases}\boldsymbol{B}=\nabla\times\boldsymbol{A},\\ \boldsymbol{E}+\dfrac{\partial\boldsymbol{A}}{\partial t}=-\nabla\varphi,\end{cases}\tag{1}$$

where $\boldsymbol{E}$ and $\boldsymbol{B}$ are the electric field vector and magnetic field vector, respectively. By substituting Equation (1) into the Maxwell equations, the wave propagation model becomes Equation (2):

$$\begin{cases}\varepsilon_0\mu_0\dfrac{\partial^2\boldsymbol{A}}{\partial t^2}-\nabla^2\boldsymbol{A}+\varepsilon_0\mu_0\dfrac{\partial(\nabla\varphi)}{\partial t}=\mu_0\boldsymbol{j},\\ \nabla^2\varphi=-\dfrac{\rho_c}{\varepsilon_0},\end{cases}\tag{2}$$

where ε_0 and μ_0 are the vacuum dielectric constant and magnetic permeability, $\boldsymbol{j}=en_e\boldsymbol{v}_e$ is the electric current density, ρ_c is the net charge, e is the elementary charge, and n_e and $\boldsymbol{v}_e$ are the electron density and velocity. The monochromatic plane wave method can be used; namely, the vectors are divided into components that are perpendicular and parallel to the wavevector. The electric field is calculated by Equation (3):

$$\begin{cases}\boldsymbol{E}_\perp=-\dfrac{\partial\boldsymbol{A}}{\partial t},\\ \dfrac{\partial\boldsymbol{E}_{//}}{\partial t}=-\dfrac{\partial\left(-\nabla_{//}\varphi\right)}{\partial t}=-\dfrac{\boldsymbol{j}}{\varepsilon_0}.\end{cases}\tag{3}$$

The $\perp$ and // symbols represent the components perpendicular and parallel to the wavevector, which indicates that $\boldsymbol{E}_{//}=E_z$ and $\boldsymbol{E}_\perp=E_x\boldsymbol{x}+E_y\boldsymbol{y}$.

The basic plasma dynamics are approximated by Equations (4) and (5):

$$\begin{cases}\dfrac{\partial n_e}{\partial t}=-\dfrac{\partial n_e v_{ez}}{\partial z},\\ \dfrac{\partial\boldsymbol{v}_e}{\partial t}=-v_{ez}\dfrac{\partial v_{ez}}{\partial z}z-\dfrac{e}{m_e}[\boldsymbol{E}+\boldsymbol{v}_e\times\boldsymbol{B}_0+\boldsymbol{v}_e\times\boldsymbol{B}]-\dfrac{\gamma_e v_{Te}^2}{n_e}\dfrac{\partial n_e}{\partial z}\boldsymbol{z}-\upsilon_e\boldsymbol{v}_e,\end{cases}\tag{4}$$

$$\begin{cases}\dfrac{\partial n_i}{\partial t}=-\dfrac{\partial n_i v_{iz}}{\partial z},\\ \dfrac{\partial\boldsymbol{v}_i}{\partial t}=\dfrac{e}{m_i}\boldsymbol{E}-\dfrac{3v_{Ti}^2}{n_i}\dfrac{\partial n_i}{\partial z}\boldsymbol{z}-\upsilon_i\boldsymbol{v}_i,\end{cases}\tag{5}$$

where the subscripts e and i represent the electron and ion, $\boldsymbol{B}$ is the magnetic field from Equation (1), n is density, $\boldsymbol{v}$ is velocity, m is mass, υ is the effective collision frequency, $v_{Te}=(k_BT_e/m_e)^{1/2}$ is the electron thermal velocity, $v_{Ti}=(k_BT_i/m_i)^{1/2}$ is the ion thermal velocity, k_B is the Boltzmann constant, and γ_e is the electron ratio of specific heats, which takes the value of 3 for high-frequency waves and the value of 1 for low-frequency waves. Variables T_e and T_i are temperatures of the electrons and ions, respectively. The ion effective collision frequency υ_i includes ion-neutral collisions and Landau damping derived from kinetic theory. The Lorentz force in the ion equations is neglected. The equations are separated into a fast timescale and a slow timescale. The electron-governed equation becomes Equation (6) for the fast timescale and Equation (7) for the slow timescale:

$$\begin{cases}\dfrac{\partial n_{eh}}{\partial t}=-\dfrac{\partial(n_{es}+n_{e0})v_{ezh}}{\partial z},\\ \dfrac{\partial\boldsymbol{v}_{eh}}{\partial t}=-\dfrac{e}{m_e}[\boldsymbol{E}_h+\boldsymbol{v}_{eh}\times\boldsymbol{B}_0-\dfrac{3v_{Te}^2}{(n_{es}+n_{e0})}\dfrac{\partial n_{eh}}{\partial z}\boldsymbol{z}-\upsilon_e\boldsymbol{v}_{eh},\end{cases}\tag{6}$$

$$m_e\frac{\partial \boldsymbol{v}_s}{\partial t} = -e\boldsymbol{E}_s - \frac{k_B T_e}{n_0}\frac{\partial n_s}{\partial z}z - \frac{e^2}{4m_e\omega_0^2}\frac{\partial|\tilde{E}_h|^2}{\partial z}z, \tag{7}$$

where subscripts h and s represent the fast timescale response and the slow timescale response, respectively. The density is governed by $n = n_0 + n_h + n_s$, where n_0, n_h, n_s represent the background density, the density fluctuations in the fast timescale, and the density fluctuations in the slow timescale, respectively. The electron background density n_{e0} equals the ion background density n_{i0}. For the slow timescale, quasi-neutrality $n_{es} = n_{is} = n_s$ is assumed, which means the velocity of the electrons and ions are the same in the slow timescale: $v_{es} = v_{is} = v_s$. The nonlinear term $n_{eh}v_{ezh}$ in the continuity equation is neglected. The nonlinear terms in the momentum equation of Equation (3) are transferred into a ponderomotive force

$$-\frac{e^2}{4m_e\omega_0^2}\frac{\partial|\tilde{E}_h|^2}{\partial z}$$

that drives the slow timescale velocity (Chen FF, 1984; Boyd and Sanderson, 2003), where $\tilde{E}_h$ is a slowly varying envelope of the high-frequency electric field and ω_0 is the pump wave frequency. Eliasson and Stenflo (2008) presented equations governing the slowly varying envelope of the high-frequency field to simulate $\tilde{E}_h$. Conversely, the high-frequency field is calculated by Equations (2), (3), and (6), and the slowly varying envelope of the high-frequency field is obtained by averaging the electric field over the fast timescale in our model.

For the ion equations, the fast timescale response is not considered, namely, $n_{ih} = 0$ and $v_{ih} = 0$ owing to the large ion mass. For the slow timescale, Equation (8) is obtained:

$$\begin{cases}\dfrac{\partial n_s}{\partial t} = -\dfrac{\partial n_0 v_{sz}}{\partial z},\\ m_i\dfrac{\partial \boldsymbol{v}_s}{\partial t} = e\boldsymbol{E}_s - m_i\dfrac{3v_{Ti}^2}{n_0}\dfrac{\partial n_i}{\partial z}\boldsymbol{z} - m_i\upsilon_i v_i,\end{cases} \tag{8}$$

where the continuity equation is linearized the same as in Equation (6). We add Equation (7) and the momentum equation in Equation (8). Equation (8) then becomes Equation (9):

$$\begin{cases}\dfrac{\partial n_s}{\partial t} = -n_0\dfrac{\partial v_{sz}}{\partial z},\\ \dfrac{\partial v_{sz}}{\partial t} = -\dfrac{C_s^2}{n_0}\dfrac{\partial n_i}{\partial z} - \upsilon_i v_{iz} - \dfrac{e^2}{4m_i m_e\omega_0^2}\dfrac{\partial|\tilde{E}_h|^2}{\partial z},\end{cases} \tag{9}$$

where the electron inertial term in Equation (7) is suppressed because of the small electron mass and $C_s = [k_B(T_e + 3T_i)/m_i]^{1/2}$ is the ion acoustic wave speed. Equations (2), (3), (6), and (9) are the equations used in the simulation.

3. Simulation Results

The parameters adopted in the simulation are as follows. In the ionospheric F_2 region, the major proportion of positive ions are oxygen atom ions. The ratio of ion mass to electron mass is m_i/m_e = 29,500. Further, $T_i = T_e$ = 1,500 K. The geomagnetic field is expressed as $\boldsymbol{B}_0 = (\boldsymbol{y}\cos\theta - \boldsymbol{z}\sin\theta)B_0$, where the y–z plane is the geomagnetic median plane and θ is the geomagnetic inclination. In this simulation, we choose a geomagnetic condition in Tromsø, Norway, where the geomagnetic inclination is approximately 78.1°, the geomagnetic field strength at ionospheric height is approximately 4.8 × 10^{-5} T and the corresponding electron gyrofrequency is 1.3466 MHz. We consider a horizontally stratified electron and ion density profile in the simulation. The profile is expressed as $n_0 = n_{\max}\exp\left[-(z - z_{\max})^2/L^2\right]$, where $z_{\max}$ = 300 km is the height of the F_2 peaks, $n_{\max} = 6.0\times10^{11}$ m^{-3} is the ionospheric maximum electron density and the corresponding plasma frequency is 6.954 MHz, and L = 40 km is the scale height. In this nonuniform nested grid method, the spatial step is set as Δz = 2 m and the total height region is selected as 200–300 km, whereas the electrostatic electric field is solved on a much denser grid size of 4 cm, at z = 271–272.92 km. The initial electric field of the pump wave is E_0 = 1 V/m. The frequency of the O-mode pump wave is 5.5 MHz. According to the O-mode dispersive relation, the pump wave is reflected at z = 272.64 km.

Figure 1 shows the simulation results for the O-mode pump wave with a frequency of 5.5 MHz. The left column shows the simulation results for the parallel electric field, electron density, and ion density in the region z = 271.96–272.536 km at t = 0.8 ms. The right column shows the simulation results at t = 1.12 ms. At t = 0.8 ms, the parallel electric field of the O-mode pump wave shows evident standing wave patterns. We can also observe fluctuations of electrons and ions simultaneously in the initial stage of parametric instability. At t = 1.12 ms, the standing wave pattern of the parallel electric field is obviously distorted because of parametric instability. More intensive disturbances of electron density and ion density can be found at the first Airy maximum of the parallel electric field.

Figure 2 shows the time evolution of the parallel electric field, electron density, and ion density. We can observe that the standing wave pattern of the electric field begins to collapse at approximately t = 1.1 ms. The parallel electric field increases to approximately 100 V/m because of Langmuir waves trapped in ion cavities. Figure 2 also shows the generation of the Langmuir turbulence contributing to the PDI. Large-amplitude fluctuations are excited first at the reflection point, and then the height of the Langmuir turbulence generated descends from 272.64 to 271.72 km with heating time. This phenomenon is consistent with the ionospheric plasma behavior during experiments at the reflection area, which descend tens of kilometers from higher to lower heights in a few minutes (Pedersen et al., 2009).

Figures 3 and 4 present the frequency spectra of the high-frequency Langmuir wave and the low-frequency ion acoustic wave during different periods at a height of 272.16 km. High-frequency spectra are calculated from the electron density, which is the disturbance from the Langmuir wave. Low-frequency spectra are calculated from the ion density, which is the disturbance from ion acoustic waves. At 0–0.727 ms, the electron density spectrum is enhanced at 5.5 MHz, which is the pump wave frequency. No obvious enhancement is observed in the ion density spectrum. The electron density spectrum at 0–0.727 ms demonstrates that the pump wave has propagated into the reflection area but that the PDI has not been excited, which is consistent with Figure 2. Subsequently, the enhanced spectrum occurs and develops at 0.727–2.182 ms at 5.456 MHz, which is the plasma frequency ω_p calculated by $\omega_p = \sqrt{(n_0 e/\varepsilon_0 m_e)}$. At the same time, the ion density

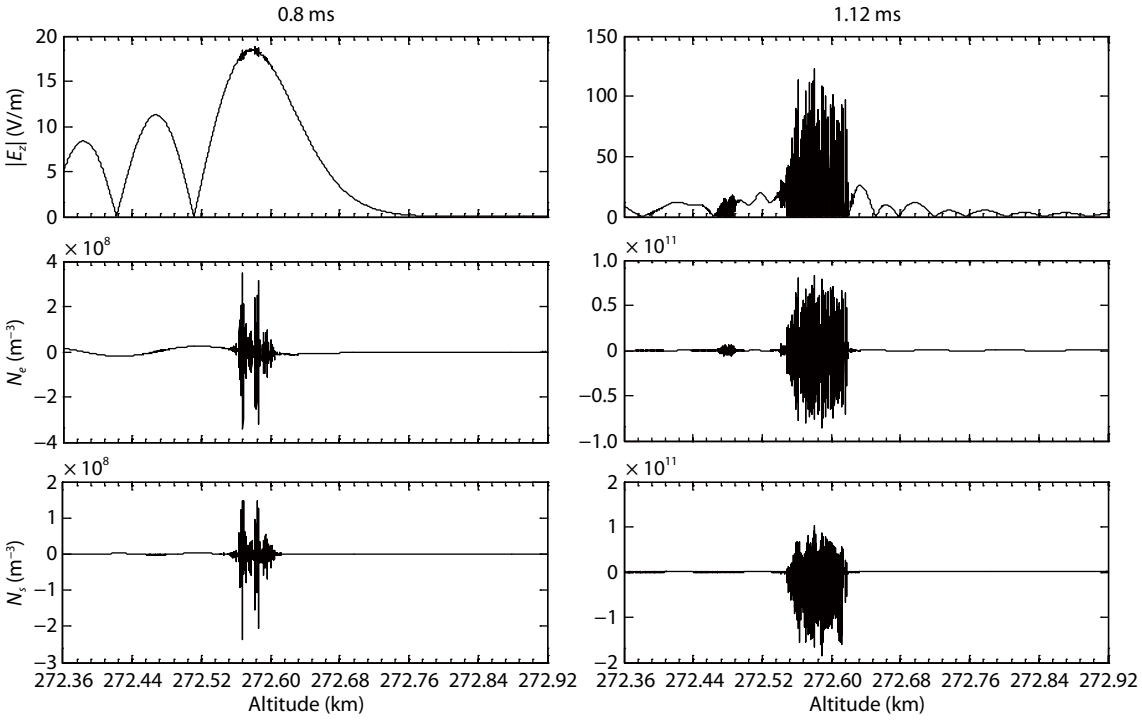

Figure 1. The parallel electric field, electron density, and ion density in the region of z = 271.96–272.536 km at time t = 0.8 ms (left column) and t = 1.12 ms (right column).

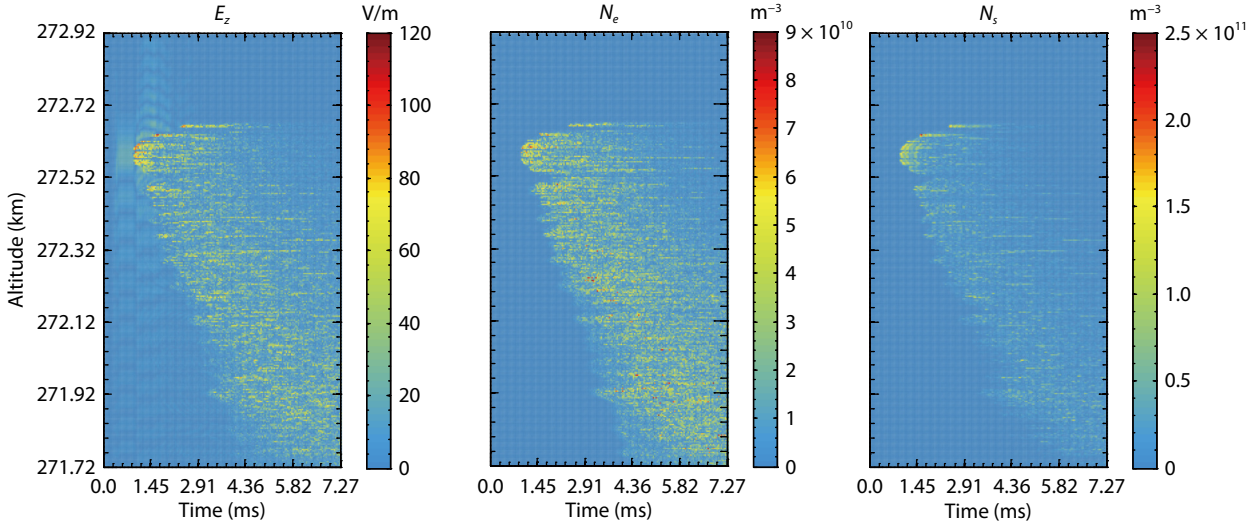

Figure 2. Time evolution of the parallel electric field (E_z), electron density (N_e), and ion density (N_s).

spectrum is slightly enhanced at 4–5.5 kHz (see Figure 4). The corresponding downshifted high-frequency enhancement is generated, but it is so slight as to be covered by the plasma oscillation with frequency ω_p.

At 2.1818–2.9091 ms (Figure 3), the enhancement at about 5.495 MHz is significant. The waves with 5.495 MHz (Figure 3) and 4–5.5 kHz (Figure 4) demonstrate that the PDI is excited because the frequency matching condition is satisfied ($\omega_p = \omega_L + \omega_{IA}$). The frequencies of electron and ion density-enhanced spectra correspond with the Langmuir wave and the ion acoustic wave. Thereafter, both the electron and ion density spectra begin to expand and the discrete spectrum becomes continuous, which is related to the cascade process and cavitons.

Figure 5 shows the time evolution of the electron and ion spectra. The process of Langmuir wave excitement and the cascade can be observed in the electron density spectrum. The high frequency expands from approximately 5.3 to 5.8 MHz. This shift may be related to the Langmuir turbulence, which causes an intensive disturbance of the electron density and an expansion of the plasma frequency. The ion acoustic wave frequency is less than 10 kHz.

The frequency matching condition is verified in this process. To further investigate the PDI process, the wavevector matching condition is studied. Figure 6 shows the simulation results for the

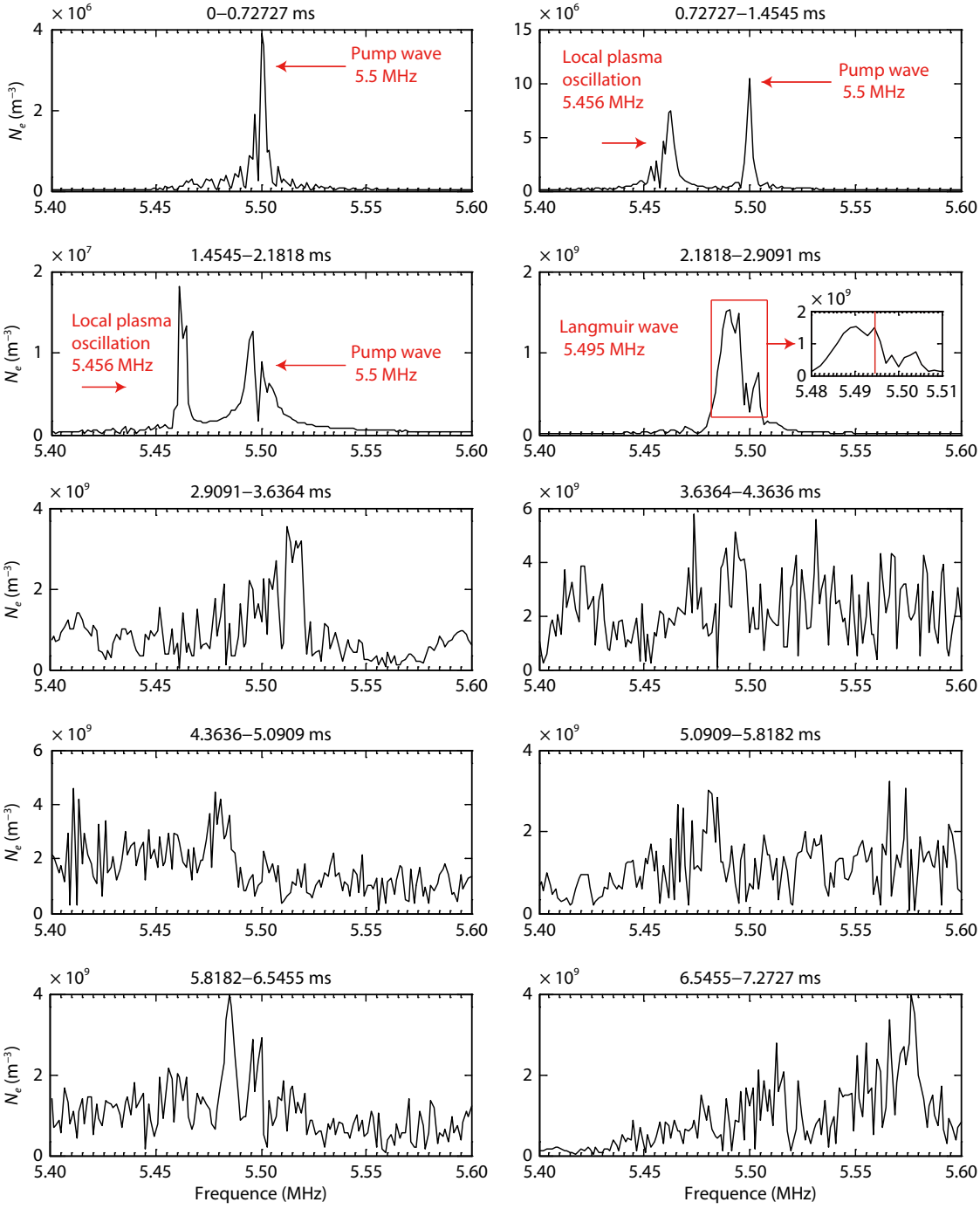

Figure 3. Frequency spectrum of the high-frequency Langmuir wave during different time periods.

parallel electric field, electron density at the fast timescale, and ion density at the slow timescale (left column), as well as the corresponding space spectra (right column) in the region z = 272.24–272.32 km at t = 1.60 ms. The standing wave pattern of the parallel electric field is obviously distorted but still visible. This result demonstrates that the Langmuir wave is excited in the region z = 272.24–272.32 km because of the PDI excitement. The small-scale structures of electron density and ion density are also excited. The space spectrum in the right column illustrates that significantly enhanced spectra of the parallel electric field, electron density, and ion density are at similar wavenumbers, which are concentrated at k_L = 14 rad/m. Near the reflection height, the wavevector of the pump wave is almost zero. Therefore, the wavevector matching condition becomes $k_1 = -k_2$, where k_1 is the Langmuir wavenumber k_L and k_2 is the ion acoustic wavenumber k_{IA}. The enhanced spectrum at a similar wavenumber corresponds with the wavevector matching condition.

Figure 7 shows the simulation results in a similar scheme as Figure 6 but at t = 1.82 ms. Here, the amplitude of small structures increases more significantly than in Figure 6 and the standing wave pattern is almost quenched. The maximum amplitude of the parallel electric field reaches about 50 V/m. The spectrum at k = 2 k_{IA} is enhanced, which is the spectral feature of the cascade. The

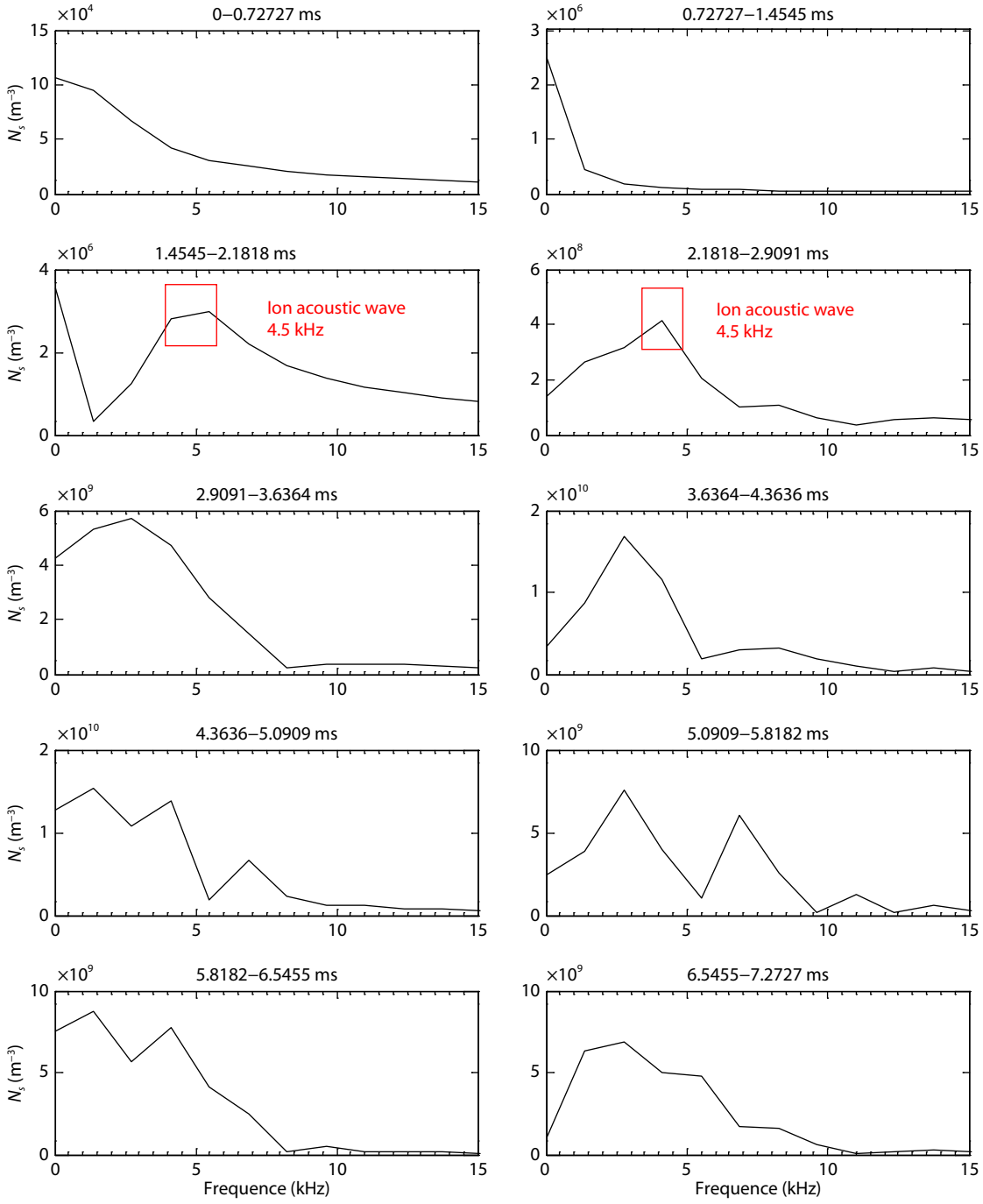

Figure 4. Frequency spectrum of the low-frequency ion acoustic wave during different time periods.

spectrum enhancement at $k = 2\ k_{IA}$ illustrates that the daughter ion acoustic wave is generated and the secondary PDI is excited. However, it is difficult to explain by the WTA and SLT theories why the daughter ion acoustic wave is stronger than the primary ion acoustic wave. Before researching this spectral feature, further development of the PDI is shown. Figure 8 shows the simulation results in a similar scheme as Figures 6 and 7 but at $t = 2.18$ ms. The maximum amplitude of the parallel electric field reaches approximately 90 V/m, and the amplitudes of the oscillations of electron and ion density grow to more than 10% of the background density. The strong cavitons have a much wider spectrum, so the enhanced spectrum shown in the right column of Figure 8 expands into more extensive wavenumbers. The spectrum at $k = 2\ k_L$ is still much more enhanced.

Figures 6 to 8 present three stages in the PDI process. The initial PDI stage refers to the enhanced spectrum at a single wavenumber, which corresponds to the first decay from the pump wave into a Langmuir wave and an ion acoustic wave, as shown in Figure 6. The Langmuir wave grows and then decays into the Langmuir sideband and acoustic wave as a pump wave. It will continue to cascade through the PDI process if the Langmuir wave generated exceeds the instability threshold. This process is the cascade stage, and the enhanced spectrum is concentrated at discrete wavenumbers, as shown in Figure 7. The final stage is

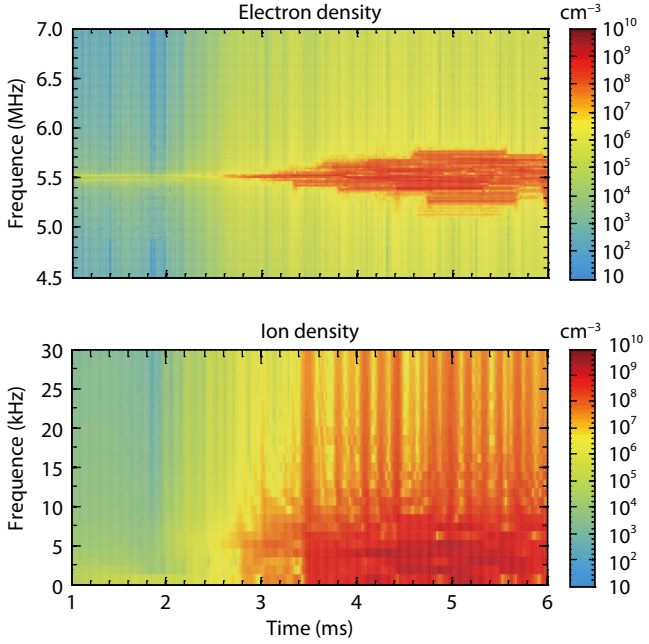

Figure 5. Simulation results of the time evolution of the electron and ion spectrum. The pump wave frequency is 5.5 MHz.

strong Langmuir turbulence generation, where the enhancement expands into a continuous spectrum, as shown in Figure 8. The ion caviton collapses and gives rise to a continuous spectrum enhancement.

Figure 9 shows simulation results of the time evolution of the wavenumber spectrum for the parallel electric field, electron density, and ion density in the region of z = 272.22–272.30 km (upper row) and z = 272.48–272.54 km (bottom row). Three stages in the PDI process can clearly be observed. In the initial PDI stage and cascade stage, the discrete spectra of electron density and ion density satisfy the wavevector matching condition. The enhanced wavenumber is different in these two areas because of the different plasma densities. In the strong Langmuir turbulence stage, enhancements expand into a full continuous spectrum. This nonlinear process is accompanied by evolution of the ion caviton, which increases to be comparable to the background ion density.

4. Discussion

The frequency and wavevector matching condition in the PDI process is studied. The PDI process can be divided into three stages: the initial PDI stage, the cascade stage, and the strong Langmuir turbulence stage. In the initial PDI stage, the high-

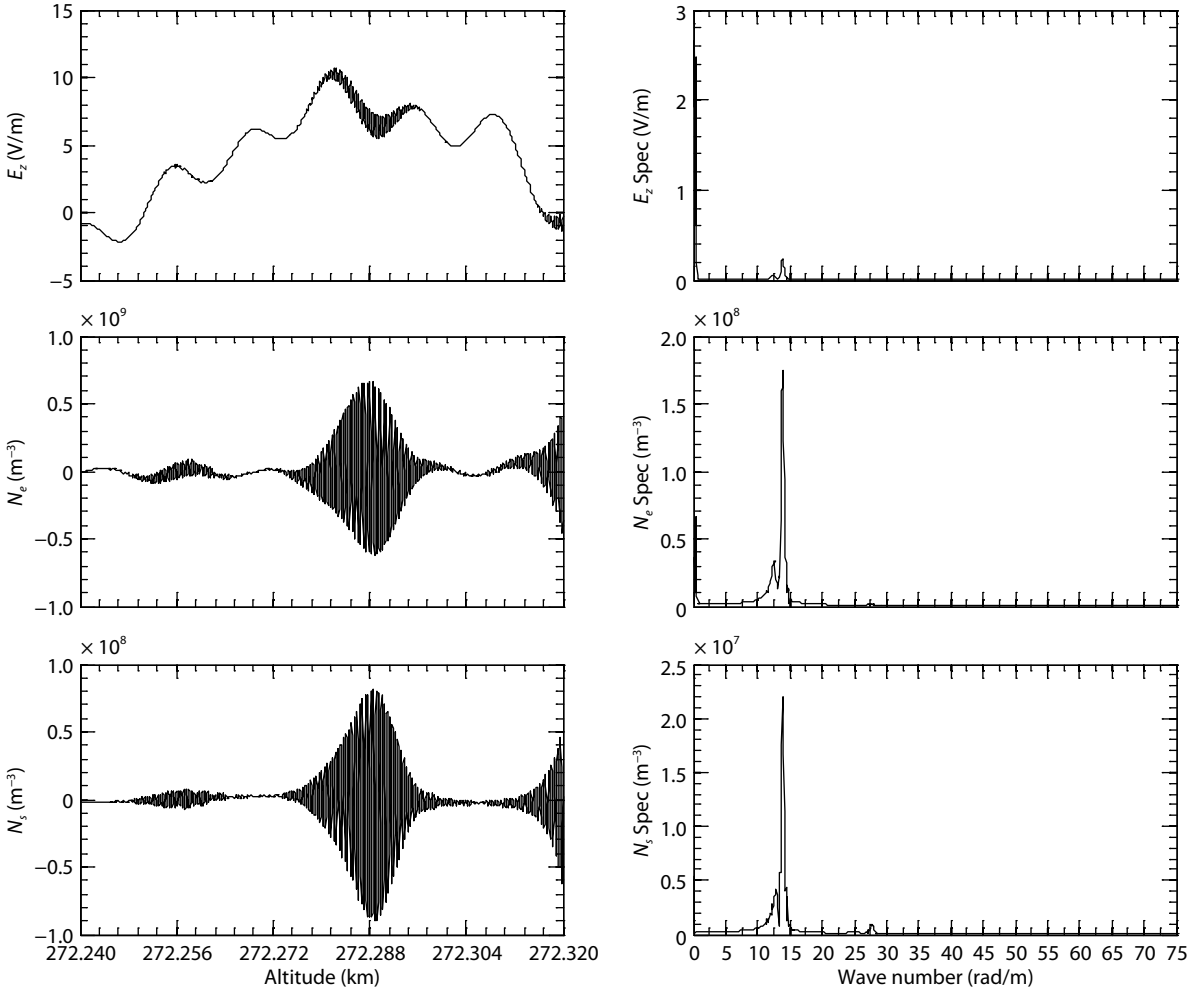

Figure 6. Simulation results of the wavenumber spectrum of the parallel electric field, electron density, and ion density at t = 1.6 ms.

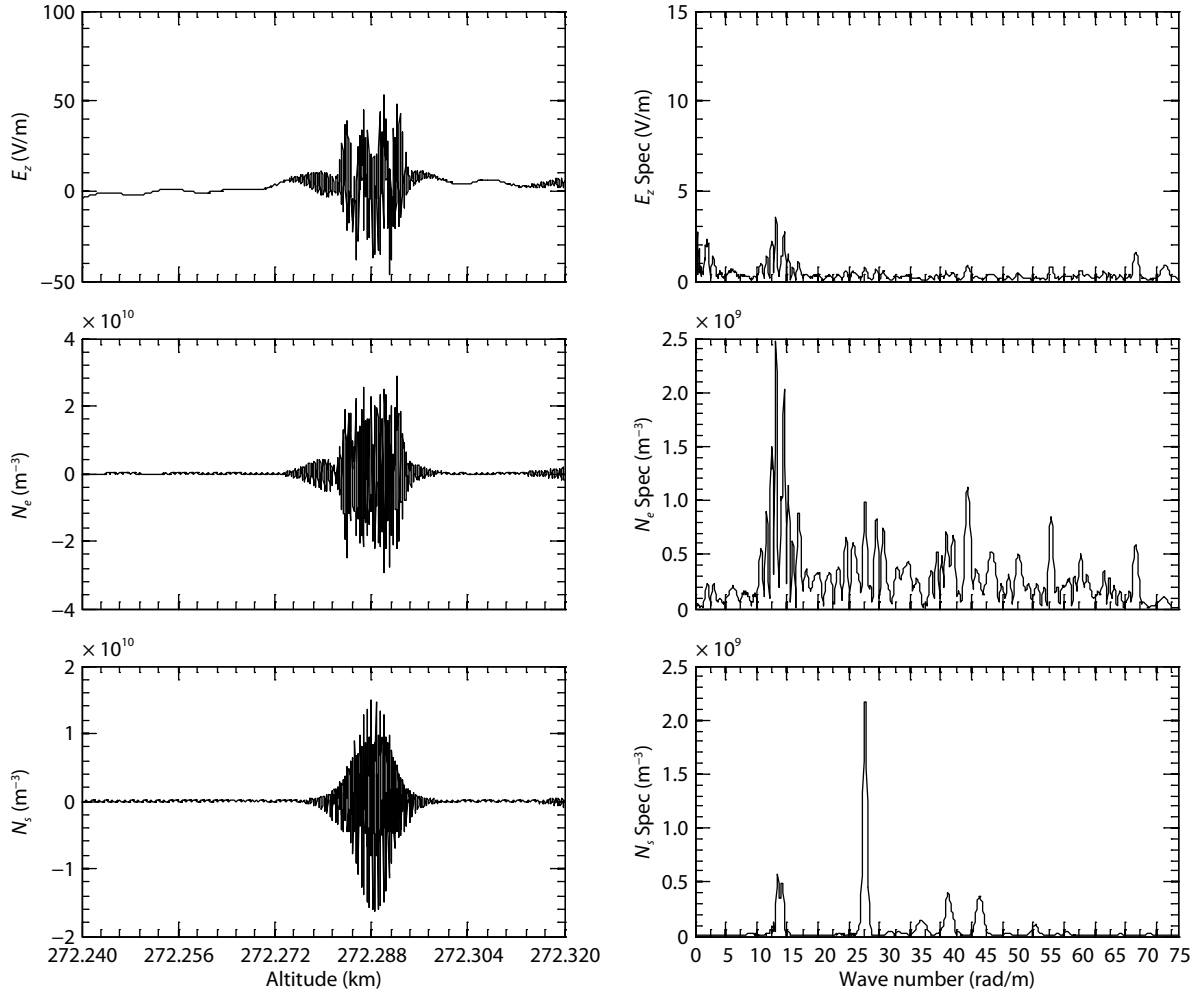

Figure 7. Simulation results of the wavenumber spectrum of the parallel electric field, electron density, and ion density at t = 1.82 ms.

frequency pump wave decays into a Langmuir wave and an ion acoustic wave. In ionospheric heating experiments, down-shifted high-frequency-enhanced plasma lines and high-frequency-enhanced ion lines observed by the incoherent scattering technique demonstrate that the PDI process is excited when the frequency and wavevector matching condition is satisfied. After the Langmuir wave is excited, the spectrum is enhanced at wavenumbers smaller than that of the Langmuir wave, which is consistent with the WTA theory (Kadomtsev, 1965; Tsytovich, 1970; Davidson et al., 1972). The Langmuir wave excited by the PDI process can grow rapidly. If the amplitude of the Langmuir wave reaches the threshold of PDI, the Langmuir wave can become a pump wave and decay into a daughter Langmuir wave and an ion acoustic wave. This decay process can be excited several times to generate a number of discrete cascade lines. The discrete enhanced spectrum agrees with the results of previous numerical analyses (Fejer and Kuo YY, 1973; Kruer and Valeo, 1973; Perkins et al., 1974).

Our simulation results show that the PDI is excited and that an initial PDI stage and a subsequent cascade stage are generated. In the initial PDI stage, the high-frequency waves at 5.495 MHz and low-frequency wave at approximately 4.5 kHz are generated at 272.16 km, which demonstrates that the frequency matching condition is satisfied. For the wavenumber spectrum, the enhancements of both the electron and ion density spectra at k = 14 rad/m from 272.22 to 272.30 km prove that the wavevector matching condition is satisfied, namely, that the matching condition in the PDI process is verified. The spectrum at smaller k than the Langmuir wavenumber is enhanced as well, which is consistent with the WTA theory (Hanssen et al., 1992).

The enhanced space spectrum at k_L = 14 rad/m demonstrates that a small-scale (0.4488 m) disturbance is generated and that the disturbance will grow to irregularities, which is consistent with prior observations (Inhester et al., 1981; Blagoveshchenskaya et al., 2011). The scales of disturbance vary at different heights. For example, as shown in Figure 9, the initial spectrum is enhanced at a smaller wavenumber in the bottom row than the upper row because the plasma density is nonuniform at various altitudes. Here, we give the theoretical frequency and wavenumber of the Langmuir and ion acoustic waves early in the linear process, which is a function of the plasma density and temperature. In the first PDI process, the frequency matching condition is as shown in Equation (10):

$$\sqrt{\omega_{pe}^2 + \frac{3}{2}k_L^2 v_{th}^2} + k_{IA}C_s = \omega_0, \tag{10}$$

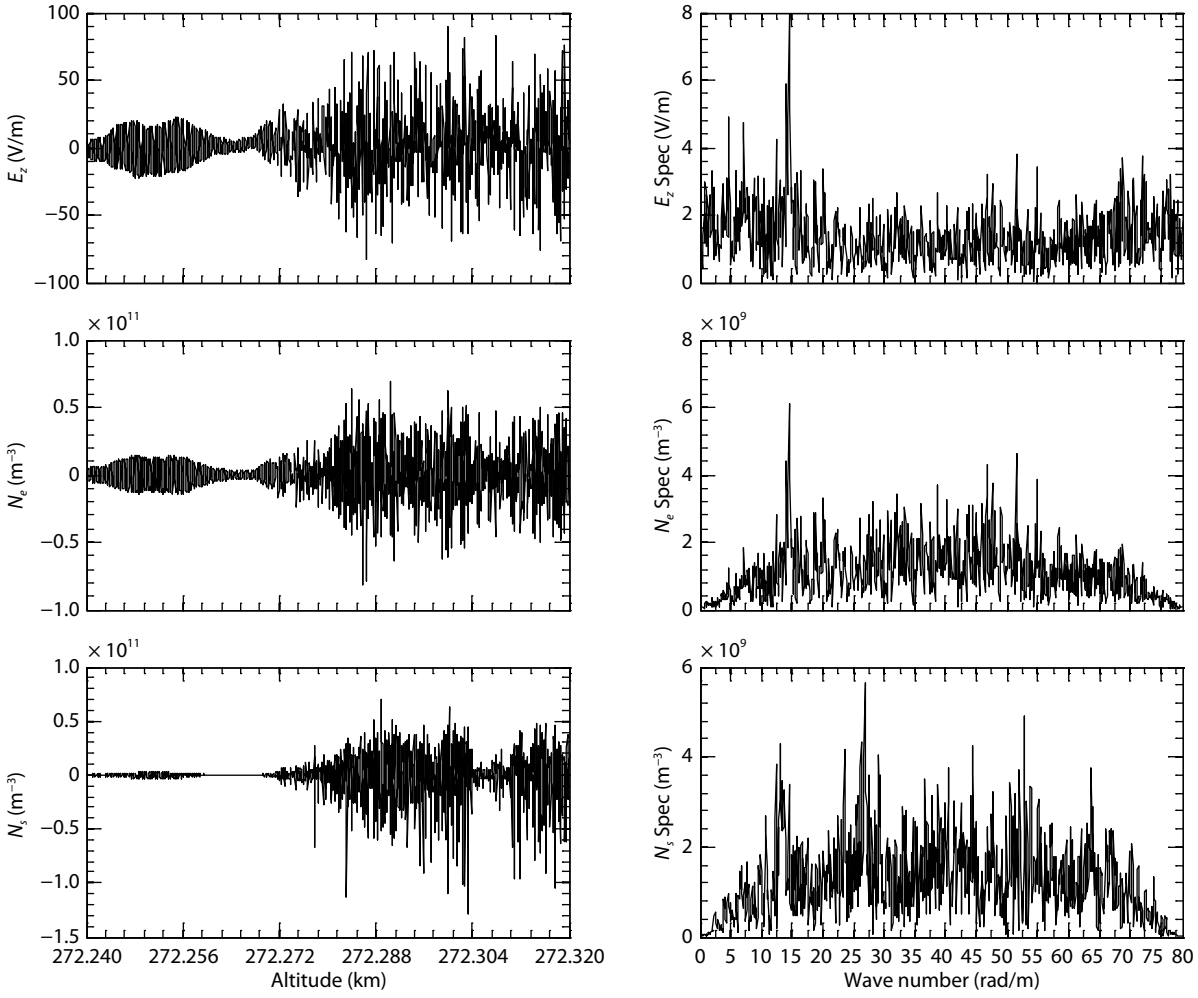

Figure 8. Simulation results of the wavenumber spectrum of the parallel electric field, electron density, and ion density at t = 2.18 ms.

where $\sqrt{\omega_{pe}^2 + \frac{3}{2}k_L^2 v_{th}^2} = \omega_L$ and $k_{IA}C_s = \omega_{IA}$ is the Langmuir wave and acoustic dispersion relation, and the v_{th} is calculated by $v_{th} = \sqrt{2k_B T_e/m_e}$. Near the reflection point, the pump wavevector is almost zero, so let $k = |k_L| = |-k_{IA}|$. Equation (10) can be solved and the wavenumber k can be obtained by Equation (11):

$$k = \frac{-2\omega_0 C_s + \sqrt{6v_{th}^2(\omega_0^2 - \omega_p^2) + 4C_s^2\omega_p^2}}{6v_{th}^2 - 2C_s^2}. \tag{11}$$

In addition, the frequencies of the Langmuir wave and ion acoustic wave can be obtained by Equation (12):

$$\begin{cases} f_L = \dfrac{\sqrt{\omega_p^2 + k^2 v_{th}^2}}{2\pi}, \\ f_{IA} = \dfrac{kC_s}{2\pi}. \end{cases} \tag{12}$$

According to Equations (11) and (12), the theoretical Langmuir wave and ion acoustic wave frequency at 272.16 km is 5.4955 MHz and 4.47 kHz, which is consistent with the simulation results shown in Figures 3 and 4. The theoretical wavenumber of the two waves can be calculated as 13.21–14.82 rad/m between 272.30 and 272.22 km and 6.54–8.65 rad/m between 272.54 and 272.48 km, which is consistent with the simulation results in Figure 9. The wavenumber k decreases with altitude, whereas the plasma temperature is constant and the density increases with altitude. The disturbance is about meter scale.

The cascade process in Langmuir parametric instability has been investigated in several studies. The maximum number of cascade lines is five, as observed by EISCAT (Westman et al., 1995). In our simulation results, the wavenumber spectrum shows the cascade process. A discrete spectrum enhancement occurs in the simulation results. The question arising from the spectral feature is that the spectrum at $k = 2\,k_L$ is much more enhanced than that at $k = k_L$, which is not consistent with the WTA prediction. Caviton formation is the most likely cause of this spectral feature. Figure 10 shows the z-direction electric field, ion density, and corresponding spectrum between 272.288 and 72.29 km at 1.6727 ms (black lines) and 1.7091 ms (red lines). Enhancements of both the Langmuir wave and the acoustic wave at k = 14.16 rad/m illustrate that the primary PDI wavevector matching condition is satisfied. The Langmuir wave spectral enhancement at k = 13.35 rad/m and the ion acoustic wave spectral enhancement at k = 27.67 rad/m demonstrate that the cascade is excited because the secondary PDI wavevector matching condition is satisfied. At t = 1.6727 ms, the cascade line of the ion acoustic wave distorts the sinusoidal ion density. The negative ion density becomes sharp, narrow, and large, which manifests as the ion density developing into cavitons. The ratio of the cascade ion line amplitude to the primary ion line

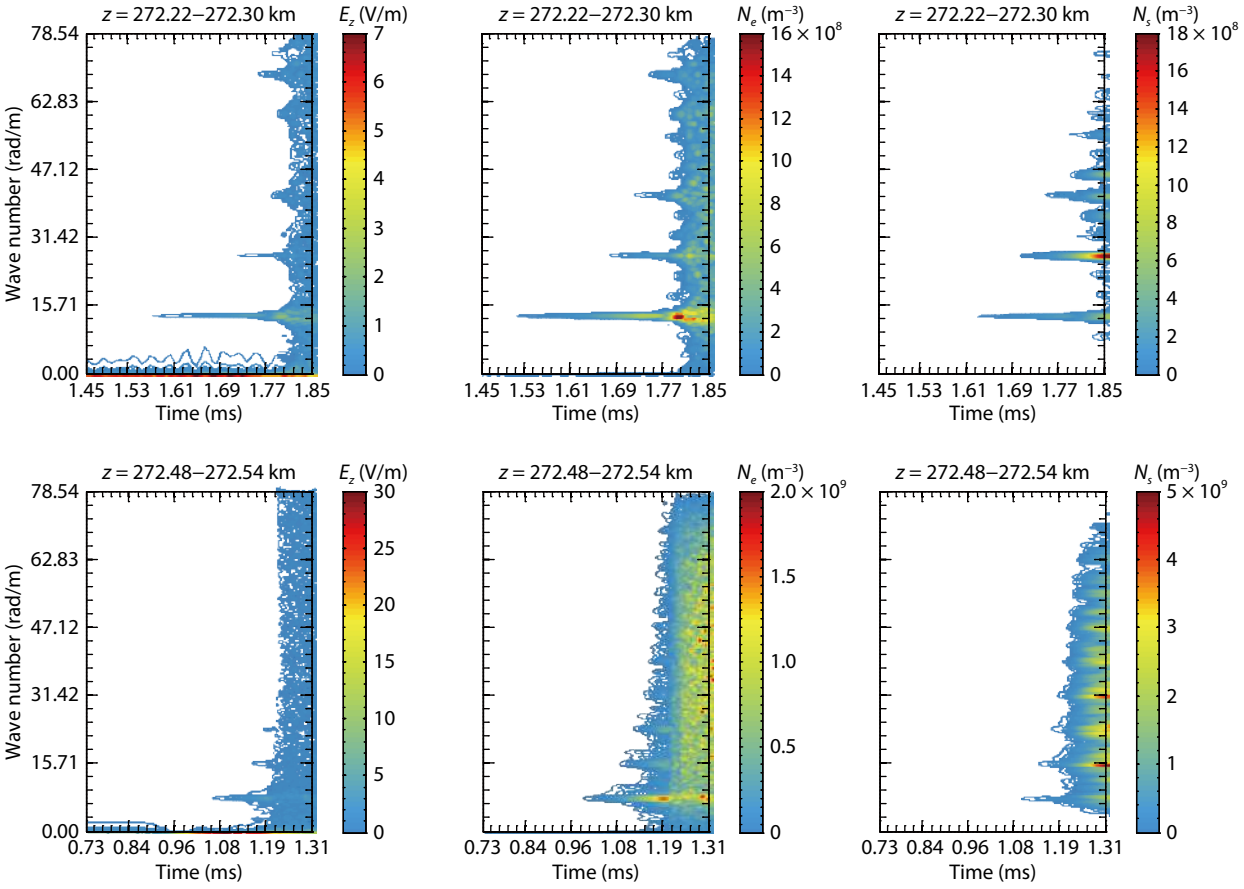

Figure 9. Simulation results of the time evolution of the wavenumber spectrum for the parallel electric field, electron density, and ion density in the region of z = 272.22–272.30 km (upper row) and z = 272.48–272.54 km (bottom row).

amplitude increases from 1/10 at 1.6727 ms to 1/3 at 1.7091 ms, which leads to a sharper and larger negative ion density. The cavitons become deeper, which can trap the electric field. Figure 10 indicates that caviton formation may be related to the cascade process. The superposition of a monochromatic wave and the second harmonics can form a caviton-shaped wave once their phase difference is –90° under the large energy of the pump wave. The cascade line at double k_L induces the development of ion density into cavitons, which trap the electric field and enhance the ponderomotive force. The cavitons then become deeper and collapse or burn out, and a strong Langmuir turbulence is excited. That is, the cascade process can induce or accelerate caviton formation and strong Langmuir turbulence excitation.

Our results present the initial PDI stage and cascade stage in detail, both of which agree with observation results. The frequency and wavevector matching conditions are evident in the first two stages. The WTA theory is valid in the initial PDI stage and the cascade process (Hanssen et al., 1992) except that the ion cascade line is more enhanced than the primary PDI ion line. DuBois et al. (1988, 1990) and Hanssen et al. (1992) presented the SLT theory based on the WTA theory. DuBois et al. (1993) observed that the SLT theory and WTA theory are applied to different areas, which means the cascade process and strong Langmuir turbulence induced by cavitons are excited at different altitudes. The area where strong Langmuir turbulence occurs is closer to the O-mode wave reflection point. DuBois et al. (1991, 1993) also presented the coexistence of cascade turbulence and caviton turbulence at certain altitudes, and they infer these types of turbulence can be attributed to the downward propagation of cavitons. Our simulation results show that the ion cascade lines can induce or accelerate the formation of cavitons and that this process may depend on the phase difference between the primary acoustic wave and the cascade acoustic wave. This result provides a potential explanation for caviton generation as a complement to the current SLT theory for caviton generation in the area where PDI and caviton turbulence coexist (DuBois et al., 1991). Our simulation results also show the continuously enhanced spectrum in the full wavenumber, and this result is closer to the saturation spectrum in observations (Hanssen et al., 1992), which demonstrates that a caviton collapse and strong Langmuir turbulence occurs. The ion cavitons grow to be comparable to the background ion density, which invalidates the linear theory. In ionospheric heating experiments, an airglow enhancement has been observed (Sipler and Biondi, 1976; Bernhardt et al., 1989). The airglow is regarded as being related to electron acceleration by strong Langmuir turbulence and a trapped electric field (Sipler and Biondi, 1976).

5. Summary

In the present study, we have investigated the evolution of Langmuir parametric instability and the generation of Langmuir turbulence in ionospheric heating by numerical simulations. We have especially focused on the analysis of frequency and wavevector

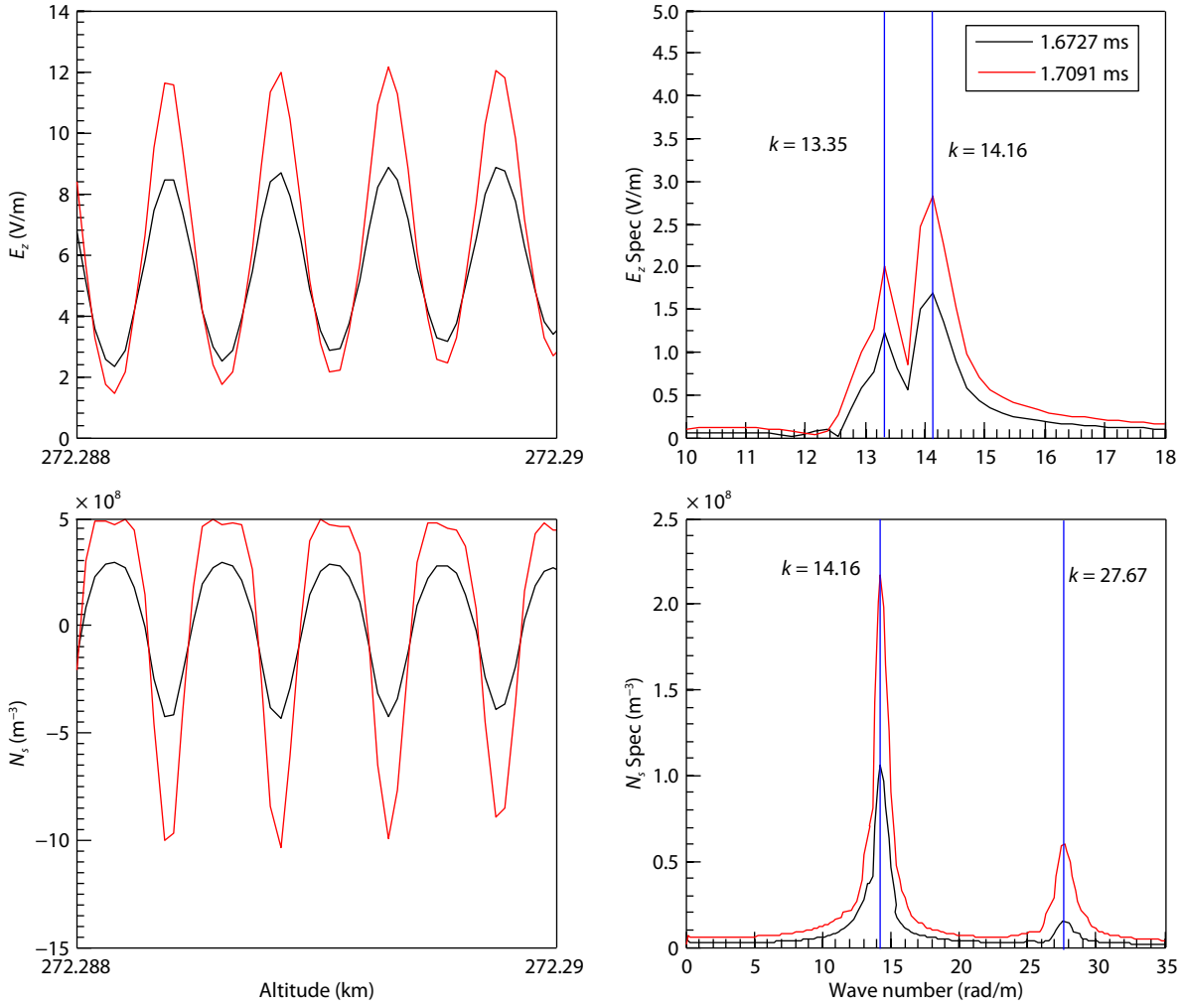

Figure 10. The *z*-direction electric field, ion density, and corresponding spectrum between 272.288 and 272.29 km at 1.6727 ms (black line) and 1.7091 ms (red line).

matching conditions by using simulation results. The principal conclusions are summarized as follows.

5.1 Frequency and Wavevector Matching Condition in the Initial Stage

Our simulation results demonstrate that PDI is excited below the O-mode pump wave reflection point after several milliseconds. The PDI occurs earlier at high altitudes because of the larger amplitude of the standing wave pattern. The Langmuir wave and acoustic wave, which both have a single frequency and wavevector, are generated in the initial PDI stage. The simulation results verify that the frequency and wavevector matching conditions are satisfied. The Langmuir wave and ion acoustic wave have different frequencies and wavenumbers at different altitudes. The frequency and wavenumber are functions of the plasma density and temperature. The simulation results show that the ion acoustic wave frequency is at a kilohertz scale and that the disturbance of plasma is at meter scale in the initial PDI stage. The analytical solution of the theoretical Langmuir and ion acoustic wave frequency and wavenumber are obtained by solving the matching condition combined with dispersion equations. The theoretical results are consistent with the simulation results.

5.2 Cascade Lines

A cascade occurred in our simulation results. After the first PDI process was excited, the Langmuir wave grew. Subsequently, the wavenumber spectrum was enhanced at an integer multiple of the Langmuir wavenumber excited in the first PDI process one by one in simulation results. The results show the process of discrete spectrum generation, namely, the cascade process. Our results are consistent with the numerical analysis of Body and Sanderson (2003). The cascade has been observed in many ionospheric heating experiments, and the simulation results are consistent with these observations.

In the cascade stage, the secondary PDI is excited and the ion density spectrum at $k'_{IA} = -2k_L$ is enhanced. The cascade acoustic wave may induce or accelerate the formation of cavitons, in which the phase difference is important. The formation of cavitons leads to a more enhanced spectrum at $k'_{IA} = -2k_L$.

5.3 Caviton Collapse and Strong Langmuir Turbulence

The simulation results in this study show that both the frequency and wavenumber spectrum expand extensively after the cascade stage. The discrete spectrum develops into a continuous spec-

trum, which indicates Langmuir turbulence excitation. Caviton collapses can also be found in our simulation, and small irregularities at 10 cm to 1 m scales are generated.

Acknowledgments

This work was supported by the National Natural Science Foundation of China (NSFC Grant Nos. 42104150, 42074187, 41774162, and 41704155), the Foundation of the National Key Laboratory of Electromagnetic Environment (Grant No. 6142403200303), the Chinese Academy of Sciences, Key Laboratory of Geospace Environment, the University of Science & Technology of China (Grant No. GE2020-01), the Fundamental Research Funds for the Central Universities (Grant No. 2042021kf0020), and the Excellent Youth Foundation of Hubei Provincial Natural Science Foundation (Grant No. 2019CFA054).

References

Akbari, H., Bhatt, A., La Hoz, C., and Semeter, J. L. (2017). Incoherent scatter plasma lines: observations and applications. *Space Sci. Rev.*, *212*(1–2), 249–294. https://doi.org/10.1007/s11214-017-0355-7

Bernhardt, P. A., Tepley, C. A., and Duncan, L. M. (1989). Airglow enhancements associated with plasma cavities formed during ionospheric heating experiments. *J. Geophys. Res.: Space Phys.*, *94*(A7), 9071–9092. https://doi.org/10.1029/JA094iA07p09071

Blagoveshchenskaya, N. F., Borisova, T. D., Yeoman, T. K., Rietveld, M. T., Ivanova, I. M., and Baddeley, L. J. (2011). Artificial small-scale field-aligned irregularities in the high latitude F region of the ionosphere induced by an X-mode HF heater wave. *Geophys. Res. Lett.*, *38*(8), L08802. https://doi.org/10.1029/2011GL046724

Blagoveshchenskaya, N. F., Borisova, T. D., Yeoman, T. K., Häggström, I., and Kalishin, A. S. (2015). Modification of the high latitude ionosphere F region by X-mode powerful HF radio waves: experimental results from multi instrument diagnostics. *J. Atmos. Sol. Terr. Phys.*, *135*, 50–63. https://doi.org/10.1016/j.jastp.2015.10.009

Blagoveshchenskaya, N. F., Borisova, T. D., Kalishin, A. S., Yeoman, T. K., and Häggström, I. (2017). First observations of electron gyro-harmonic effects under X-mode HF pumping the high latitude ionospheric F-region. *J. Atmos. Sol. Terr. Phys.*, *155*, 36–49. https://doi.org/10.1016/j.jastp.2017.02.003

Boyd, T. J. M., and Sanderson, J. J. (2003). Particle orbit theory. In T. J. M. Boyd, et al. (Eds.), *The Physics of Plasmas* (pp. 12–47). Cambridge: Cambridge University Press. https://doi.org/10.1017/CBO9780511755750.003

Bryers, C. J., Kosch, M. J., Senior, A., Rietveld, M. T., and Yeoman, T. K. (2013). The thresholds of ionospheric plasma instabilities pumped by high-frequency radio waves at EISCAT. *J. Geophys. Res.: Space Phys.*, *118*(11), 7472–7481. https://doi.org/10.1002/2013JA019429

Carlson, H. C., Gordon, W. E., and Showen, R. L. (1972). High frequency induced enhancements of the incoherent scatter spectrum at Arecibo. *J. Geophys. Res.*, *77*(7), 1242–1250. https://doi.org/10.1029/JA077i007p01242

Chen, F. F. (1984). *Introduction to Plasma Physics and Controlled Fusion*. New York: Plenum Press.

Cheung, P. Y., Sulzer M. P., DuBois D. F., and Russell, D. A. (2001). High-power high-frequency-induced Langmuir turbulence in the smooth ionosphere at Arecibo. II. Low duty cycle, altitude-resolved, observations. *Phys. Plasmas*, *8*(3), 802–812. https://doi.org/10.1063/1.1345704

Dahl, T., and Murphree, D. (1972). Numerical solution for propagation of longitudinal waves along the geomagnetic field using a three-fluid ionosphere model. *IEEE Trans. Antennas Propag.*, *20*(6), 807–809. https://doi.org/10.1109/TAP.1972.1140335

Davidson, R. C., Hammer, D. A., Haber, I., and Wagner, C., E. (1972). Nonlinear development of electromagnetic instabilities in anisotropic plasmas. *Phys. Fluids*, *15*(2), 317–333. https://doi.org/10.1063/1.1693910

DuBois, D. F., Rose, H. A., and Russell, D. (1988). Power spectra of fluctuations in strong Langmuir turbulence. *Phys. Rev. Lett.*, *61*(19), 2209–2212. https://doi.org/10.1103/PhysRevLett.61.2209

DuBois, D. F., Rose, H. A., and Russell, D. (1990). Excitation of strong Langmuir turbulence in plasmas near critical density: application to HF heating of the ionosphere. *J. Geophys. Res.: Space Phys.*, *95*(A12), 21221–21272. https://doi.org/10.1029/ja095ia12p21221

DuBois, D. F., Rose, H. A., and Russell, D. (1991). Coexistence of parametric decay cascades and caviton collapse at subcritical densities. *Phys. Rev. Lett.*, *66*(15), 1970–1973. https://doi.org/10.1103/PhysRevLett.66.1970

DuBois, D. F., Hanssen, A., Rose, H. A., and Russell, D. (1993). Space and time distribution of HF excited Langmuir turbulence in the ionosphere: comparison of theory and experiment. *J. Geophys. Res.: Space Phys.*, *98*(A10), 17543–17567. https://doi.org/10.1029/93JA01469

DuBois, D. F., Russell, D. A., Cheung, P. Y., and Sulzer, M. P. (2001). High-power high-frequency-induced Langmuir turbulence in the smooth ionosphere at Arecibo I. Theoretical predictions for altitude-resolved plasma line radar spectra. *Phys. Plasmas*, *8*(3), 791–801. https://doi.org/10.1063/1.1345703

Eliasson, B., and Stenflo, L. (2008). Full-scale simulation study of the initial stage of ionospheric turbulence. *J. Geophys. Res.*, *113*(A2), A02305. https://doi.org/10.1029/2007JA012837

Eliasson, B., and Stenflo, L. (2010). Full-scale simulation study of stimulated electromagnetic emissions: the first ten milliseconds. *J. Plasma Phys.*, *76*(3–4), 369–375. https://doi.org/10.1017/S0022377809990559

Fejer, J. A., and Kuo, Y. Y. (1973). Structure in the nonlinear saturation spectrum of parametric instabilities. *Phys. Fluids*, *16*(9), 1490–1496. https://doi.org/10.1063/1.1694546

Fejer, J. A. (1979). Ionospheric modification and parametric instabilities. *Rev. Geophys.*, *17*(1), 135–153. https://doi.org/10.1029/RG017i001p00135

Feng, T., Liu, M. R., and Zhou, C. (2018). Investigation on matching conditions of Langmuir parametric instability in ionospheric heating. In *2018 12th International Symposium on Antennas, Propagation and EM Theory (ISAPE)* (pp. 1–2), Hangzhou, China: IEEE. https://doi.org/10.1109/ISAPE.2018.8634128

Hagfors, T., Kofman, W., Kopka, H., Stubbe, P., and Äijanen, T. (1983). Observations of enhanced plasma lines by EISCAT during heating experiments. *Radio Sci.*, *18*(6), 861–866. https://doi.org/10.1029/RS018i006p00861

Hanssen, A., Mjølhus, E., DuBois, D. F., and Rose, H. A. (1992). Numerical test of the weak turbulence approximation to ionospheric Langmuir turbulence. *J. Geophys. Res.: Space Phys.*, *97*(A8), 12073–12091. https://doi.org/10.1029/92JA00874

Inhester, B., Das, A. C., and Fejer, J. A. (1981). Generation of small-scale field-aligned irregularities in ionospheric heating experiments. *J. Geophys. Res.: Space Phys.*, *86*(A11), 9101–9106. https://doi.org/10.1029/JA086iA11p09101

Jiang, C. H., Wei, L. H., Yang, G. B., Zhou, C., and Zhao, Z. Y. (2020). Numerical simulation of the propagation of electromagnetic waves in ionospheric irregularities. *Earth Planet. Phys.*, *4*(6), 565–570. https://doi.org/http://doi.org/10.26464/epp2020059

Kadomtsev, B. B. (1965). *Plasma Turbulence*. New York: Academic Press.

Kruer, W. L., and Valeo, E. J. (1973). Nonlinear evolution of the decay instability in a plasma with comparable electron and ion temperatures. *Phys. Fluids*, *16*(5), 675–682. https://doi.org/10.1063/1.1694402

Kuo, S. P., Lee, M. C., and Kossey, P. (1997). Excitation of oscillating two stream instability by upper hybrid pump waves in ionospheric heating experiments at Tromsø. *Geophys. Res. Lett.*, *24*(23), 2969–2972. https://doi.org/10.1029/97GL03054

Kuo, S. P. (2001). Cascade of the parametric decay instability in ionospheric heating experiments. *J. Geophys. Res.: Space Phys.*, *106*(A4), 5593–5597. https://doi.org/10.1029/2000JA000240

Kuo, S. P. (2003). Parametric excitation of lower hybrid waves by electron plasma waves. *Phys. Lett. A*, *307*(4), 244–248. https://doi.org/10.1016/S0375-9601(02)01601-8

Kuo, S. P. (2014). Overview of ionospheric modification by high frequency (HF) heaters-theory. *Prog. Electromagn. Res. B*, *60*(1), 141–155. https://doi.org/10.2528/PIERB14041805

Kuo, S. P. (2015). Ionospheric modifications in high frequency heating experiments. *Phys. Plasmas*, *22*(1), 012901. https://doi.org/10.1063/

1.4905519

Leyser, T. B. (1991). Parametric interaction between upper hybrid and lower hybrid waves in heating experiments. *Geophys. Res. Lett.*, *18*(3), 408–411. https://doi.org/10.1029/91gl00136

Liu, Y., Zhou, C., Xu, T., Tang, Q., Deng, Z. X., Chen, G. Y., and Wang, Z. K. (2021). Review of ionospheric irregularities and ionospheric electrodynamic coupling in the middle latitude region. *Earth Planet. Phys.*, *5*(5), 462–482. https://doi.org/10.26464/epp2021025

Nguyen, B. T., Furse, C., and Simpson, J. J. (2015). A 3-D stochastic FDTD model of electromagnetic wave propagation in magnetized ionosphere plasma. *IEEE Trans. Antennas Propag.*, *63*(1), 304–313. https://doi.org/10.1109/TAP.2014.2365824

Pedersen, T., Mishin, E., and Esposito, R. (2009). New observations of HF-induced optical emissions from the ionospheric *E* region. *J. Geophys. Res.*: *Space Phys.*, *114*(A6), A06316. https://doi.org/10.1029/2008JA013596

Perkins, F. W., and Kaw, P. K. (1971). On the role of plasma instabilities in ionospheric heating by radio waves. *J. Geophys. Res.*, *76*(1), 282–284. https://doi.org/10.1029/JA076i001p00282

Perkins, F. W., Oberman, C., and Valeo, E. J. (1974). Parametric instabilities and ionospheric modification. *J. Geophys. Res.*, *79*(10), 1478–1496. https://doi.org/10.1029/JA079i010p01478

Rietveld, M. T., Isham, B., Kohl, H., La Hoz, C., and Hagfors, T. (2000). Measurements of HF-enhanced plasma and ion lines at EISCAT with high-altitude resolution. *J. Geophys. Res.*: *Space Phys.*, *105*(A4), 7429–7439. https://doi.org/10.1029/1999JA900476

Rush, C. (1986). Ionospheric radio propagation models and predictions—a mini-review. *IEEE Trans. Antennas Propag.*, *34*(9), 1163–1170. https://doi.org/10.1109/TAP.1986.1143951

Sipler, D. P., and Biondi, M. A. (1976). Enhanced O I 6300-Å regions produced by the Platteville ionospheric modification experiment. *J. Geophys. Res.*, *81*(19), 3467–3470. https://doi.org/10.1029/JA081i019p03467

Song, B., Wong, A. Y., Villaseñor, J., Rosenthal, G., McCarrick, M., Pau, J., and Sentman, D. (1995). Experimental study of double resonance parametric excitations in the ionosphere. *Radio Sci.*, *30*(6), 1875–1883. https://doi.org/10.1029/95RS01729

Stenflo, L. (1985). Parametric excitation of collisional modes in the high-latitude ionosphere. *J. Geophys. Res.*, *90*(A6), 5355–5356. https://doi.org/10.1029/JA090iA06p05355

Stubbe, P., Kohl, H., and Rietveld, M. T. (1992). Langmuir turbulence and ionospheric modification. *J. Geophys. Res.*, *97*(A5), 6285–6297. https://doi.org/10.1029/91JA03047

Tsytovich, V. N. (1970). *Nonlinear Processes in a Plasma*. New York: Plenum Press.

Wang, X., Zhou, C., Liu, M. R., Honary, F., Ni, B. B., and Zhao, Z. Y. (2016). Parametric instability induced by X-mode wave heating at EISCAT. *J. Geophys. Res.*: *Space Phys.*, *121*(10), 10536–10548. https://doi.org/10.1002/2016JA023070

Wang, X., and Zhou, C. (2017). Aspect dependence of Langmuir parametric instability excitation observed by EISCAT. *Geophys. Res. Lett.*, *44*(18), 9124–9133. https://doi.org/10.1002/2017GL074743

Westman, A., Leyser, T. B., Wannberg, G., and Rietveld, M. T. (1995). Tristatic EISCAT-UHF measurements of the HF modified ionosphere for low background electron temperatures. *J. Geophys. Res.*: *Space Phys.*, *100*(A6), 9717–9728. https://doi.org/10.1029/94JA03337